



Dynamic oxygen storage modeling in a three-way catalyst for natural gas engines: A dual-site and shrinking-core diffusion approach



Jian Gong*, Di Wang, Junhui Li, Neal Currier, Aleksey Yezerets

Corporate Research and Technology, Cummins Inc., 1900 McKinley Avenue, Columbus, IN 47201, United States

ARTICLE INFO

Article history:

Received 2 September 2016

Received in revised form 28 October 2016

Accepted 2 November 2016

Available online 5 November 2016

Keywords:

Three-way catalyst

Oxygen storage capacity

Natural gas engine

Kinetic modeling

Shrinking core diffusion

ABSTRACT

A dual-site oxygen storage model was developed to predict the dynamic oxygen storage on a Pd/Rh/CeZrO_x TWC catalyst. Two oxygen storage sites (surface and sub-surface) were used to describe two distinct regimes of the oxygen storage process. A shrinking core diffusion model was applied on the sub-surface site to predict slow oxygen storage and depletion. It is found that water gas shift and steam reforming reactions play significant roles in determining the oxygen storage capacity (OSC) and they were included in the model. A methodology of OSC measurement was designed to quantify the OSC with distinct reductants over a temperature window of 250 °C to 650 °C for model development. The amount of OSC with different reductants were compared. The reducibility of the reductants on OSC decreased in the order of H₂ > CO > CH₄. The amount of OSC showed a slight temperature dependency when using H₂, followed by CO and CH₄ in the temperature from 250 °C to 450 °C. However, similar amount of OSC was observed when the temperature was above 450 °C regardless of the reductants. With the dual-site OSC model, the dynamic oxygen storage capacities with various reductants could be correctly predicted.

© 2016 Elsevier B.V. All rights reserved.

1. Introduction

1.1. Oxygen storage components in TWC

Three-way catalytic converter (TWC) has been widely and successfully utilized in stoichiometric gasoline and natural gas engines to control pollutants such as carbon monoxide (CO), hydrocarbons (HC) and nitrogen oxides (NO_x) in the last decades [1,2]. It is well known that a TWC has a maximum conversion efficiency in a narrow window around stoichiometric air fuel ratio (AFR), where all the major pollutants can be simultaneously reduced. Maintaining the AFR around the stoichiometric condition is quite challenging. In real world operating conditions, deviation from the stoichiometric conditions (fuel cut and acceleration) were often encountered. Therefore, oxygen storage components (Ceria or Ceria and Zirconia solution) were introduced in the TWCs for effective AFR control. The main function of OSC is to act as an oxygen buffer to extend the operating window of the AFRs and help to curb emission breakthrough. With the aid of oxygen storage components, better performance can be achieved by dithering such that the AFR is targeting to a specific mean value rather than holding to that

value constantly. Also, CO and NO conversions can be enhanced when AFR switches between lean and rich exhaust composition [2,3]. The secondary benefits including promotion of the water gas shift (WGS) and steam reforming reactions, increasing the thermal stability of the support, improving precious metal dispersion, were extensively reviewed in the literature [4,5].

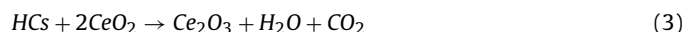
It is well established that the dynamic OSC is a result of reduction of ceria at rich and reoxidation of ceria at lean. A large number of studies on the reduction of CeO₂ have been collected by temperature programmed reduction (TPR) measurements on ceria containing materials [6–8] as well as ceria supported precious metals catalysts [7,9,10], which provide insights into temperature dependent interactions between reductants and CeO₂. These TPR studies indicated that there are multiple steps of ceria reduction depending on the catalyst temperature. For ceria supported precious metal catalysts, the reduction of ceria occurs firstly on the precious metal and ceria interface at low temperatures (~350 K) [7,11] and progressively takes place on the sub-surface at higher temperatures through migration of oxygen vacancies [12]. Bulk ceria reduction was observed at very high temperature (~1100 K) [7]. It was also found that the reducibility of the ceria is essentially determined by the textural and morphological properties of ceria [4,13]. For example, a higher reducibility of ceria was observed on the cubic structure ceria compared to the tetragonal and monoclinic ceria, which was attributed to a higher oxygen mobility on the cubic

* Corresponding author at: Corporate Research and Technology, Cummins Inc., 1900 McKinley Ave., M/C 50183, Columbus, IN 47201, United States.
E-mail address: jian.gong@cummins.com (J. Gong).

Nomenclature

A_i	Pre-exponential factor
E_i	Activation energy (kJ/mol)
θ_i	CeO ₂ coverage of the i^{th} site
$R_{i,\text{surf}}$	Reaction rate of specie i at the PGM/ceria surface site (mole/m ³ -s)
$R_{i,\text{sub}}$	Reaction rate of specie i at the sub-surface site (mole/m ³ -s)
c_i	Concentration of specie i (mole/m ³)
Ω_i	Site density of the i^{th} site (mole/m ³)
k_{if}	Reaction rate constant of the i^{th} forward reaction (m ³ /mole-s)
k_{ib}	Reaction rate constant of the i^{th} backward reaction (m ³ /mole-s)
$k_{i,\text{eff}}$	Effective reaction rate constant of the i^{th} reaction (m ³ /mole-s)
$K_{i,\text{eq}}$	Equilibrium constant of i^{th} reaction (–)
K_i	Adsorption equilibrium constants (–)
ΔG	Change of gibbs free energy (kJ/mol)
ΔH	Change of enthalpy formation (kJ/mol)
ΔS	Change of entropy formation (kJ/mole-K)
l_D	Diffusion rate scale (s/m)
d_p	Diameter of CeO ₂ particle (m)
D	Diffusion coefficient of oxygen from surface to sub-surface (m ² /s)
OS_t	Cumulative oxygen storage at time t (μmole O/g catalyst)
SV	Space velocity at standard condition (1/s)
P	Ambient pressure (Pa)
R	Universal gas constant (J/mole-K)
T	Catalyst temperature (K)
m_{cat}	Mass of the catalyst (g)
V_{cat}	Volume of the catalyst (m ³)
r_t	Radius of total ceria particle (m)
r_s	Radius of sub-surface ceria particle (m)

structure [14]. Also, the degree of CeO₂ reduction at reducing conditions depends on the type of reductant and temperature. Eqs. (1)–(3) shows the OSC reduction reactions under reducing conditions using H₂, CO and HCs as reductants.



Under oxidizing conditions, oxygen is stored by filling up the oxygen deficient sites on the precious metal as well as the most active ceria surface. In the meantime, oxygen lattice on the surface ceria can diffuse into the sub-surface ceria and bulk ceria through intermediates O₂[–] (superoxide) and O₂^{2–} (peroxide) in the process of O₂ dissociation [15]. Diffusion can be a rate limiting factor of dynamic OSC in fast redox cycling experiments [6]. Eq. (4) shows the global reaction when O₂ is exposed to the reduced ceria under oxidizing conditions.



1.2. Modeling activities towards OSC

Since TWC catalyst performance is strongly correlated to the dynamic OSC, development of a dynamic OSC model is very crucial for modeling the TWC catalyst performance behaviors. There is a number of OSC models available in the literature, which include

simplified control-orientated models, global kinetic models as well as detailed microkinetic models. Brinkmeier et al. lumped oxygen storage and release into a single global reaction in the TWC model, which was able to predict the dynamic lambda signal of a commercial TWC [16]. Similarly, a control-orientated OSC model was developed by Kumar et al. [17] to simulate the oxygen storage in a TWC by lumping all the reducing species into one single representative specie. Koltsakis et al. is one of the pioneer researchers who first incorporated a global OSC model into TWC modeling in order to improve the model accuracy during transient conditions [18]. Later on, the OSC model was extended by considering H₂, CO and HCs as reducing species and O₂ and NO as oxidizing species [19]. This extended OSC model was extensively used in the modeling of TWC by many other researchers [20–22]. Surprisingly, most of the OSC models did not take into account of the effect of H₂O and CO₂, which were founded to be weaker oxidizers of Ce₂O₃ compared to O₂. Holder et al. incorporated the OSC reactions with H₂O and CO₂ independently in his model, however, thermodynamic consistency was not discussed [23]. Moller et al. [24] is probably the first researcher to systematically investigate the effects of H₂O and CO₂ on the OSC in TWCs through experiments and modeling. In his work, the effects of H₂O and CO₂ on OSC was experimentally observed and modeled, however, WGS reaction was not modeled independently but lumped into his OSC model. In most of detailed microkinetic TWC models [25–27], kinetics of oxygen storage and release on ceria were not included at all but lumped together with the kinetics of precious metals. Some microkinetic TWC models [28–30] were found to be able to predict the dynamic performance of TWC by incorporating an additional oxygen storage site beside the precious metal site. In normal operation of TWC, the single OSC site modeling approach was adequate to capture the TWC performance without taking into account of the slow oxygen storage due to oxygen lattice diffusion. However, in some circumstances such as fuel cut events, the oxygen storage can be significantly higher compared to the normal dithering due to the extra oxygen storage on the subsurface or in bulk ceria.

In the present study, a dynamic oxygen storage model was developed in a TWC for natural gas engines. Thermodynamically consistent kinetics were presented and discussed which take into account the effect of H₂O and CO₂. Model validations on the experimental OSC data collected on a tube flow reactor was discussed.

2. Experiments

2.1. Catalyst

The catalyst used in this study was a three way catalyst containing precious metals supported on ceria/zirconia (CeZrO_x). The catalytically active material was coated on a cordierite monolith with a cell density of 400 cells per square inch (cps) and wall thickness of 0.102 mm. The catalyst was de-greened by 5% O₂ in presence of 5% CO₂ and 5% H₂O at 650 °C for 1 h. No specific pretreatment was carried on the catalyst sample. Oxygen storage capacity (OSC) measurements were performed on the de-greened sample with a diameter of 1/4 inch and a length of 1 inch.

2.2. Methodologies of OSC measurements

A fix-bed quartz tube reactor system was used for the OSC measurements. All the simulated exhaust concentration were introduced by MKS mass flow controllers from three different gas banks. Lean gas bank consists of O₂ and N₂. Rich gas bank consists of different reductants, such as H₂, CO or CH₄. Common bank consists of CO₂ and H₂O. Helium was used as the carrier gas for all the other gases. A fast switching valve was used to switch

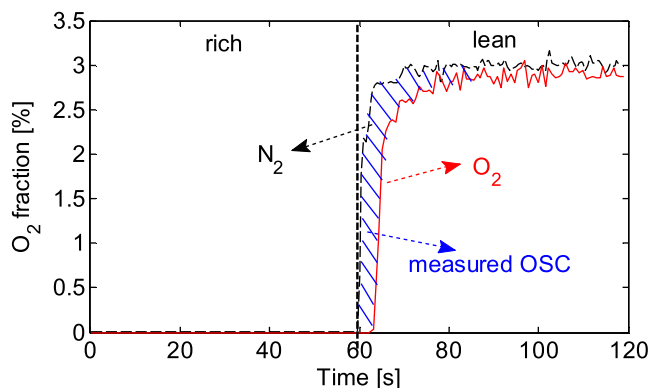


Fig. 1. O_2 fraction during OSC lean/rich cycling experiments for OSC measurement.

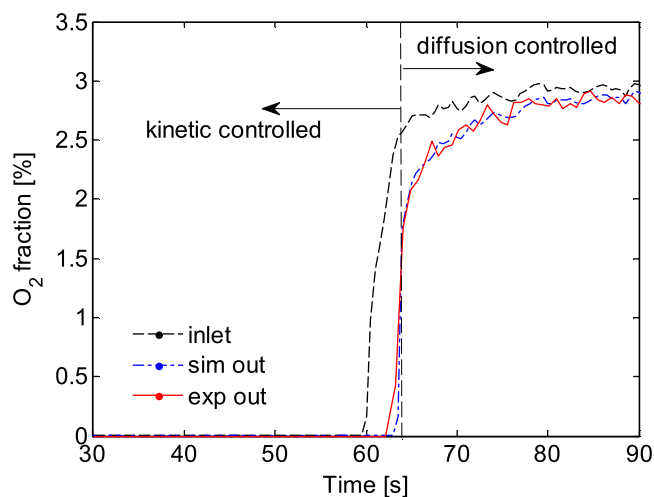


Fig. 2. Comparison of oxygen mole fraction at the outlet of the catalyst between the model and experiments (H_2 as reductant at a temperature of $400^\circ C$).

the feeding gas between lean and rich gas banks. All the effluent gas concentrations were measured by a Hiden mass spectrometer. Specifically, $m/e=32$ and $m/e=2$ were used for O_2 and H_2 concentration measurements, respectively. More detailed information about this micro-reactor system can be found in [31,32].

OSC measurement was performed under dynamic switches between lean and rich at a specific temperature. The duration of lean and rich period was 60 s. Even though TWCs are generally operated at a much shorter lean/rich cycling period, it was found that 60 s was necessary to saturate the oxygen storage during the lean period in the present study as shown in Fig. 1. During rich operation, the valve was switched to rich bank with 2.5% reductants (H_2 , CO or CH_4). At lean operation, the valve was switched to the lean bank with 3% O_2 , 5% CO_2 and 5% H_2O were presented in both lean and rich conditions in order to mimic the realistic engine exhaust conditions. N_2 was used as the rich-lean transition tracer to simulate the inlet O_2 concentration and reactor system response. The amount of OSC was calculated by integrating the difference between N_2 and O_2 signal during the lean cycle. Fig. 1 shows an example of OSC measurement during a lean/rich cycling experiment. The area between the N_2 and O_2 signal accounts for the amount of OSC. A constant space velocity of 25000 h^{-1} was applied for all the tests. The OSC measurements were conducted at each temperature under isothermal conditions. Negligible temperature increase was observed at the outlet of the catalyst. This is probably due to the limited heat generated due to the relatively small OSC of this catalyst. The temperature window under investigation is from $250^\circ C$ to $650^\circ C$ with an increment of $50^\circ C$. At

each temperature, the OSC measurement with the lean and rich cycling was repeated for 15 times. Also, “blank tube” (without catalyst) OSC measurements were conducted at each temperature to eliminate any artificial effect introduced by instruments. The value of OSC reported in the following study were intrinsic value after subtracting the blank tube OSC.

3. Modeling

A single-channel, one-dimensional model was developed to describe the monolith converter with the following assumptions: 1) steady state; 2) axisymmetric geometry; 3) neglect axial diffusion of mass and heat axial Peclet number, defined as the ratio of axial diffusion time to the axial convection time, is about 1000 for heat and mass transport, which indicates the dominance of the convective heat and mass transfer [33]. The governing equations for mass, energy conservation and species transport equations can be found in [34]. Bulk mass transfer was included to account for mass transfer between bulk gas and washcoat by assuming that the reaction rate is equal to the diffusion rate using the classic “film” model. Based on the OSC kinetics in the present study, the importance of the washcoat diffusion was evaluated from kinetic and mass transfer resistance analysis [35,36]. It was found that, over the temperature between $250^\circ C$ and $650^\circ C$, kinetic resistance is much higher than the washcoat diffusion resistance. Therefore, washcoat diffusion was neglected in the model, which was adopted in several other OSC modeling studies [19,24].

3.1. Oxygen storage and depletion on PGM-ceria surface

Oxygen chemisorption on precious metals is known to be very fast and comparable to O_2 storage on surface ceria [7]. Precious metals increase the OSC in a ceria supported precious metal catalyst due to the synergistic reduction of ceria in close contact with the precious metal [7,37,38]. The reducibility of the ceria is significantly enhanced in the presence of precious metal. The consequence is that in the presence of a precious metal, reduction of surface CeO_2 occurs at much lower temperatures. On the other hand, the addition of zirconia promotes the reduction of CeO_2 . The introduction of ZrO_2 strongly modified the reduction behavior of CeO_2 by shifting main H_2 consumption to a lower temperature, which was evidenced by H_2 TPR experiments [6,9]. The promotion of reduction was attributed to the enhanced oxygen mobility of solid solutions compared to pure oxides.

Considering the complicated composition of ceria containing material in a TWC and strong interactions between ceria, zirconia and precious metals, it is almost impossible to distinguish the contribution of each component to the overall oxygen storage. Also, it was found that the amount of oxygen chemisorbed on the precious metals is much smaller compared with ceria [7]. Therefore, oxygen storage on precious metal and surface ceria were lumped together in our model.

One oxygen storage site (S_1) was used to represent the precious metal and surface ceria active sites for rapid oxygen storage and depletion. The Arrhenius equation was applied to describe the rate constant:

$$k_i = A_i \exp\left(-\frac{E_i}{RT}\right) \quad (5)$$

where A_i is the pre-exponential factor and E_i is the activation energy. The extent of oxidation of the oxygen storage component is defined by Eq. (6).

$$\theta_1 = \frac{2 \times \text{mole of } CeO_2}{2 \times \text{mole of } CeO_2 + \text{mole of } Ce_2O_3} \quad (6)$$

The fraction of vacant site for oxygen storage was calculated as $1 - \theta_1$. Therefore, the rate expression for oxygen storage on the PGM and ceria surface site can be described by Eq. (7), where Ω_1 is the site density of S1.

$$R_{O_2, surf} = k_{1f} c_{O_2} \Omega_1 (1 - \theta_1) \quad (7)$$

During the rich operation of the TWC, H_2 and CO are the most reactive species to deplete the stored O_2 . Therefore, kinetics of OSC depletion by H_2 and CO need to be considered. In addition, many studies have reported that H_2O [39–41] and CO_2 [42,43] were able to oxidize reduced ceria in addition to oxygen, even though oxygen was a more effective oxidizer. These findings indicated that the equilibrium oxidation state of ceria component could be affected by the presence of H_2O and CO_2 in the engine exhaust. In other words, the backward reactions of OSC depletion by H_2 and CO have to be considered in the model. Miller et al. [24,44] reported for the first time that both H_2O and CO_2 splitting over a ceria/zirconia (CZ) composition from experimental observation and modeling. In order to have a thermodynamically consistent kinetic model, equilibrium constants calculated from thermodynamic properties were used to model the backward reactions.

$R_{H_2, surf} = k_{2f} c_{H_2} \Omega_1 \theta - k_{2b} c_{H_2O} \Omega_1 (1 - \theta_1)$ (8) where $k_{2b} = \frac{k_{2f}}{K_{2,eq}}$ and $K_{i,eq}$ is the equilibrium constant, which can be evaluated from Eq. (9).

$$K_{i,eq} = \exp\left(-\frac{\Delta G}{RT}\right) \quad (9)$$

And ΔG is the change of Gibbs free energy, which is calculated from $\Delta G = \Delta H - T\Delta S$. Similarly, the rate expression for OSC depletion by CO is shown in Eq. (10) by considering the effect of CO_2 .

$$R_{CO, surf} = k_{3f} c_{CO} \Omega_1 \theta - k_{3b} c_{CO_2} \Omega_1 (1 - \theta_1) \quad (10)$$

It is worth mentioning here that self-reduction of CeO_2 was not considered in the model. In other words, only the forward reaction of $Ce_2O_3 + 0.5O_2 \rightarrow CeO_2$ was modeled. This is because the O_2 releasing reaction from CeO_2 is thermodynamically favored only at very high temperatures (>1300 K), which are far beyond of typical engine exhaust temperatures [45,46].

3.2. Oxygen storage and depletion on sub-surface ceria

Besides oxygen storage and depletion on the PGM and ceria surface sites, additional sites at the edges of CZ crystallites and at the sub-surface of the ceria could contribute to the oxygen storage as well [47,48]. The kinetics and the density of active sites of the sub-surface can be significantly different compared to that of the surface site due to different physicochemical properties. The dominating mechanism of oxygen storage and depletion on the sub-surface ceria was diffusion [4,8,13].

In order to model the oxygen diffusion from surface site to the sub-surface site, a shrinking core diffusion model [49,50] was developed with following assumptions: (1) ceria is a spherical particle with an outer layer of CeO_2 and an inner core of Ce_2O_3 ; (2) the outer layer of CeO_2 is very thin; (3) oxygen lattice needs to be diffused into the inner core of Ce_2O_3 (oxygen vacancies) to store oxygen. Based on these assumptions, the final rate expression of oxygen storage on the sub-surface site is shown in Eq. (11) with an effective rate constant in Eq. (12). Detailed derivation of Eq. (12) is documented in Appendix A.

$$R_{O_2, sub} = k_{4f, eff} c_{O_2} \Omega_2 (1 - \theta_2) \quad (11)$$

$$k_{4f, eff} = \frac{k_{4f}}{1 + k_{4f} \left[1 - (1 - \theta_2)^{1/3} \right] l_D} \quad (12)$$

In Eq. (12), $l_D = \frac{d_p}{D}$, D is the diffusion coefficient of between the surface ceria and sub-surface ceria and d_p is the diameter of the ceria particle. A value of 7.8E–9 m was used to represent the diameter of the ceria particle of a fresh sample according to [51]. The diffusion coefficient was calibrated based on the OSC experiments, which will be discussed in the following section.

Similarly, OSC depletion by H_2 and CO on sub-surface sites are assumed to be diffusion limited. Oxygen lattice needs to diffuse from the sub-surface site back to the surface site to react with H_2 and CO at the surface. The rate expression for OSC depletion by H_2 and CO on this second site are described by Eqs. (13) and (14) with an effective reaction constant shown in Eq. (15). To be consistent with the equilibrium reactions on the surface ceria site discussed above, backward reactions were considered as well. The equilibrium constants were calculated from Eq. (9).

$$R_{H_2, sub} = k_{5f, eff} c_{H_2} \Omega_2 \theta_2 - k_{5b, eff} c_{H_2O} \Omega_2 (1 - \theta_2) \quad (13)$$

$$R_{CO, sub} = k_{6f, eff} c_{CO} \Omega_2 \theta_2 - k_{6b, eff} c_{CO_2} \Omega_2 (1 - \theta_2) \quad (14)$$

$$k_{i, eff} = \frac{k_i}{1 + k_i \left[1 - (1 - \theta_2)^{1/3} \right] l_D} \quad (i = 5f, 5b, 6f, 6b) \quad (15)$$

3.3. Kinetics of OSC

It is challenging to obtain the intrinsic kinetic parameters of the OSC reactions as the oxygen uptake at lean and depletion at rich conditions are very fast even at 250 °C. This is especially true for $CeZrO_x$ supported precious metal catalysts. Therefore, the kinetic parameters on the surface ceria site and sub-surface site were calibrated based on the experimental OSC data in this study. The kinetics were calibrated separately on the surface site and sub-surface site based on the assumption that the redox kinetics of the sub-surface site is much slower than that of the surface site. The calibrated kinetic parameters of the OSC reactions on surface and sub-surface ceria are given in Table 1.

On the surface oxygen storage site, the oxygen storage kinetics were calibrated based on oxygen concentrations during breakthrough at different temperatures in the kinetic controlled regime. The calibrated activation energy of oxygen uptake on the surface site is 25 kJ/mole, which is quite consistent with the reported value of 21 kJ/mol by Holmgren et al. [52]. Generally, the activation energy for Ce_2O_3 oxidation is low. A zero activation energy was used by Mukadi et al. in his microkinetic model [28]. An activation energy of 10 kJ/mol was obtained by Moller et al. [24]. Brinkmeier et al. obtained a value of 11.3 kJ/mol from OSC measurements using lambda sensors on a gasoline engine. For CeO_2 reduction by H_2 , the calibrated activation energy is 45 kJ/mol based on the H_2 concentrations during breakthrough at various temperatures. From literatures, the activation energy of H_2 oxidation on precious metals varied from 29 to 54 kJ/mol [53–55], while the activation energy of H_2 oxidation on $CeZrO_x$ was reported from 62 to 88 kJ/mol [40,47]. It can be seen that the calibrated H_2 oxidation activation energy is close to that of precious metals. For the reaction of CeO_2 reduction by CO, the activation energy was calibrated to be 65 kJ/mole, which is within the range of 30–70 kJ/mol on $CeZrO_x$ supported precious metal catalysts [9,56].

On the sub-surface sites, different kinetics compared to that of PGM-surface site were used. Generally, it is quite challenging to resolve the kinetics on sub-surface ceria. It was widely reported that the morphology and micro-structure between surface ceria (closely contact with PGM) and sub-surface ceria are quite different. These two active sites have intrinsically different activities. Therefore, the kinetics of bulk ceria from literatures was assumed to represent the kinetics on the sub-surface ceria in the model. Specifically, the activation energy of the reactions were taken from the literatures and

Table 1
Kinetic parameters for OSC storage and depletion on the model TWC.

NO.	Sites	Reaction	A_{if} [m ³ /mole-s]	E_{if} [kJ/mole]	References
1	S1	$Ce_2O_3 + 0.5O_2 \rightarrow 2CeO_2$	$1.78E+04$	25.00	this work
2	S1	$H_2 + 2CeO_2 \leftrightarrow Ce_2O_3 + H_2O$	$1.02E+07$	45.00	this work
3	S1	$CO + 2CeO_2 \leftrightarrow Ce_2O_3 + CO_2$	$3.16E+06$	65.00	this work
4	S2	$Ce_2O_3 + 0.5O_2 \rightarrow 2CeO_2$	$1.00E+08$	67.00	[58]
5	S2	$H_2 + 2CeO_2 \leftrightarrow Ce_2O_3 + H_2O$	$1.58E+07$	62.50	[40]
6	S2	$CO + 2CeO_2 \leftrightarrow Ce_2O_3 + CO_2$	$4.68E+09$	85.00	[21]

$\Omega_1 = 30 \text{ mol/m}^3$, $\Omega_2 = 50 \text{ mol/m}^3$

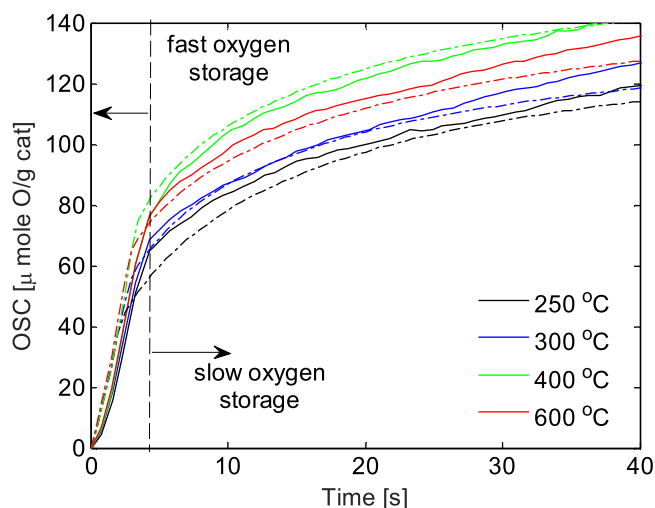


Fig. 3. Cumulative oxygen storage after 60 s using H_2 as reductant at 250 °C, 300 °C, 400 °C and 600 °C (dash line: model; solid line: experiments).

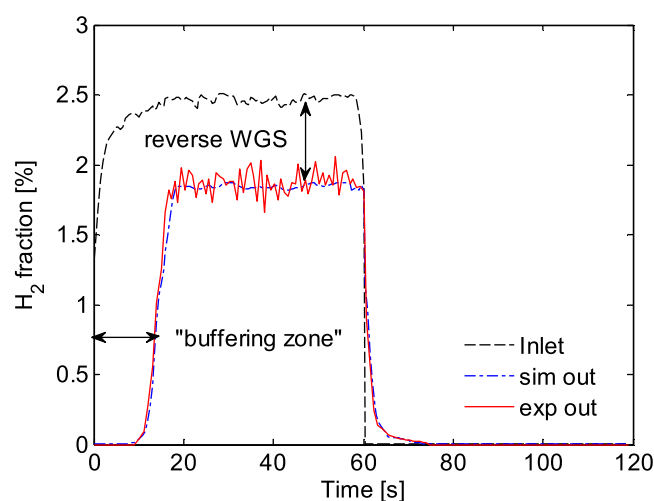


Fig. 5. H_2 fraction during the rich period of a H_2/O_2 alternatively pulsing experiment at 600 °C.

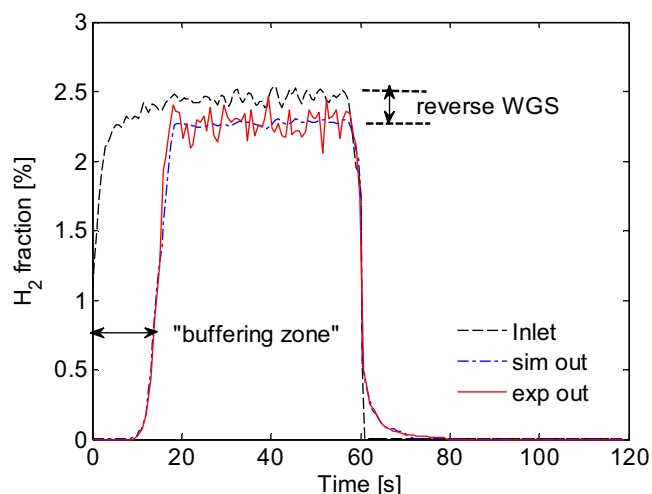


Fig. 4. H_2 fraction during the rich period of a H_2/O_2 alternatively pulsing experiment at 400 °C.

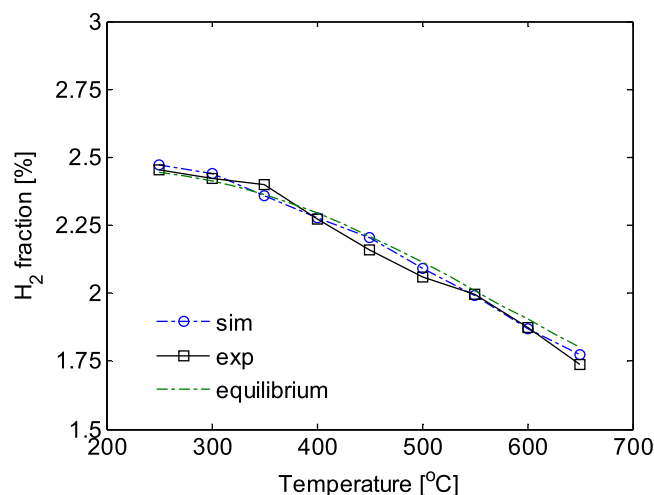


Fig. 6. TWC outlet H_2 fractions as a function of temperature at steady state conditions (inlet H_2 fractions 2.5% with 5% CO_2 and 5% H_2O).

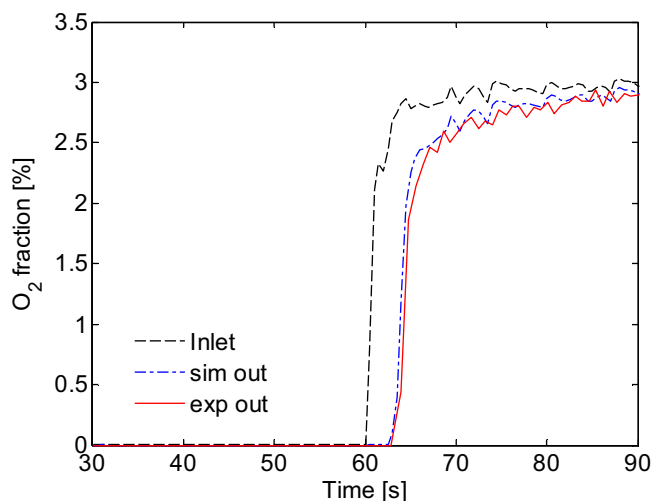
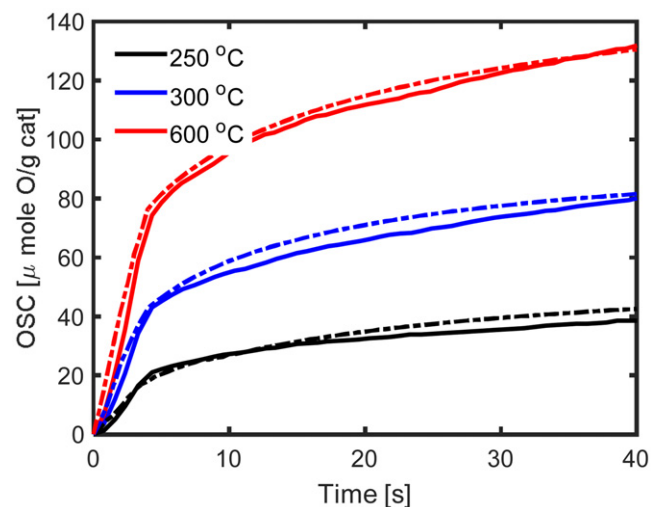
the pre-exponential factors were calibrated based on the experimental data. Through the calibrations, it was found that the kinetics of OSC on sub-surface site are not very sensitive to the model predictions in the slow oxygen storage regime since diffusion is the dominant mechanism. Therefore, the diffusion coefficient was calibrated based on the oxygen concentration at various temperatures during the diffusion controlled regime. As it can be seen in Fig. 3, the slopes of cumulative oxygen storage profiles at different temperatures were very close, indicating a temperature independent diffusion rate. Similar trends were observed in Fig. 8 and Fig. 9 for CO and CH_4 respectively. Therefore, a constant value of $8.0e-11 \text{ m}^2/\text{s}$ was used and was found to be adequate to capture the slow oxy-

gen storage characteristics. This value is reasonably close to the reported value of $3.1e-12 \text{ m}^2/\text{s}$ for polycrystalline CeO_2 , according to Steele et al. [57].

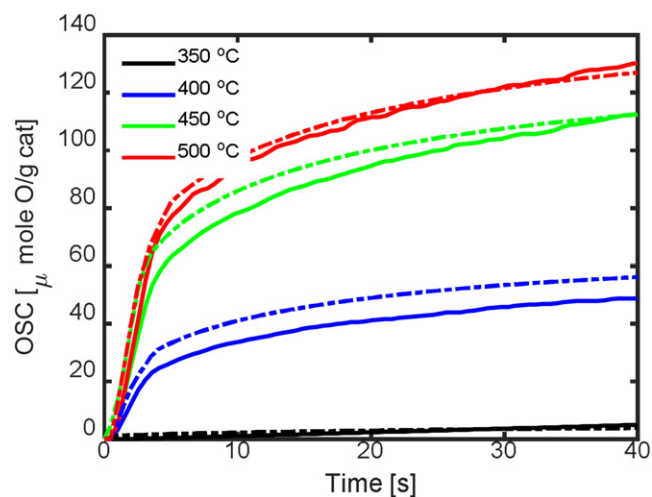
In order to correctly capture the temperature dependence of OSC and derive a thermodynamic consistent kinetic model, the thermodynamic properties of the oxygen storage components need to be estimated and calibrated. The thermodynamic properties of CZ solid solutions depend primarily on the composition of the oxides and the extent of ceria reduction [59]. A large variability of their chemical and textural properties has been reported [60,61]. From thermodynamics, it is the change of enthalpy and entropy formation that determines the thermodynamic equilibrium of the

Table 2Kinetic parameters for water-gas-shift reaction and CH₄ steam reforming reaction.

NO.	Sites	Reaction	A [m ³ /mole-s]	E (kJ/mol)
7	PGM	CO + H ₂ O ↔ CO ₂ + H ₂	3.55E+9	109.7
8	PGM	CH ₄ + H ₂ O ↔ CO + 3H ₂	1.0E+07	87.0
$K_{CO} = 8.75 \cdot 10^{-10} \exp\left(\frac{6969}{T}\right)$ [63]				
$K_{H_2} = 3.98 \cdot 10^{-8} \exp\left(\frac{4639}{T}\right)$ [63]				
$K_{wgs,eq} = \exp\left(-25.8 + \frac{24798}{T}\right)$ [63]				
$K_{sr,eq} = \exp\left(5.06 - \frac{4652}{T}\right)$ [63]				

**Fig. 7.** Comparison of oxygen fraction at the outlet of the catalyst between the model and experiments (CO as reductant at a temperature of 400 °C).**Fig. 8.** Cumulative oxygen storage after 60 s using CO as reductant at three different temperatures (dash line: model; solid line: experiments).

reaction. A correlation equation between the change of enthalpy and CeO₂ coverage was derived by Moller et al. to fit the experimental data while the change of entropy was fitted to be a constant. In order to simplify the calibration process, the thermodynamic properties of Ce₂O₃ were assumed to be constants while the enthalpy formation and entropy of CeO₂ were calibrated. The standard molar enthalpy of formation and standard molar entropy of the Ce₂O₃ were taken from the tabulated data of the bulk Ce₂O₃ [62]. The calibrated thermodynamic properties of CeO₂ were given in Table 3 and compared to the reported values from literature. It can be seen

**Fig. 9.** Cumulative oxygen storage after 60 s using CH₄ as reductant at 350 °C, 400 °C, 450 °C and 500 °C (dash line: model; solid line: experiments).**Table 3**

Thermodynamic properties of cerium oxides.

Composition	$\Delta^f H_0$ [kJ/mole]	$\Delta^f S_0$ [J/mole-K]	References
Ce ₂ O ₃	−1796.2	150.6	[62]
CeO ₂	−1088.7	62.3	[62]
Ce _{0.5} /Zr _{0.5} O _{2-x}	−1100 to −1000	55–79	[59]
CeO ₂ (sub-surface)	−1040	40	this work
CeO ₂ (surface)	−1020	80	this work

that the calibrated thermodynamic properties are comparable to those reported in the literature.

4. Results and discussions

4.1. OSC with H₂ as a reductant

In the first step, the dynamic oxygen storage and depletion was studied by alternatively feeding H₂ and O₂ to the catalyst at a constant catalyst temperature. In the first 60 s, H₂ was fed into the catalyst and the oxygen stored on the catalyst was removed by consuming H₂. From 60 to 120 s, O₂ was introduced into the catalyst and chemisorbed on the catalyst (precious metal surface, ceria surface and sub-surface and probably bulk ceria), resulting in a delay of the oxygen signal at the outlet of the catalyst.

Fig. 2 shows the result of oxygen storage process during the lean period. There was a complete oxygen uptake period about 3 s followed by oxygen breakthrough, which implies a fast oxygen storage on the surface ceria site. After the breakthrough, the outlet oxygen fraction did not reach the inlet oxygen level until 80 s. During this period, oxygen was continually chemisorbed at a much slower rate indicating a relatively slow oxygen storage on the sub-surface of the ceria, which is diffusion controlled. It can be seen that a good agreement between the model and experiment can be achieved

with the shrinking core diffusion model on the sub-surface site, which suggests that modeling oxygen lattice diffusion is necessary to predict the dynamic OSC.

In order to investigate the dynamic change of oxygen storage, cumulative oxygen storage was calculated according to Eq. (16). Again, the cumulative OSC curves from the “blank tube” OSC tests were subtracted to eliminate any artificial impacts.

$$OS_t = \frac{SV}{m_{cat}} \int_{t=60s}^t 2 (c_{O_2,in} - c_{O_2,out}) \frac{PV_{cat}}{RT} dt \quad (16)$$

Cumulative oxygen storages at three different temperatures are shown in Fig. 3. Clearly, there are two distinct stages during the oxygen storage process: fast oxygen storage and slow oxygen storage. From 0 to 5 s, the oxygen storage linearly increased with time. Beyond 5 s, the amount of oxygen storage increased slowly. The similar slopes of the oxygen storage with respect to time at different temperatures during the slow oxygen storage regime indicates that the diffusion rate is weakly dependent on temperature. Furthermore, these two different stages agree with the kinetic controlled regime and diffusion controlled regime indicated in Fig. 2.

Fig. 4 shows the H_2 fraction at the TWC outlet during the rich operation at temperature of 400 °C. When the gas was switched from lean to rich, there was a “buffering zone” right after the switch resulting in a delay of H_2 signal. This delay is due to the reaction between H_2 and stored oxygen. A good agreement of the H_2 fraction between the model and experiments indicates that the amount of OSC was correctly predicted by the model. After the “buffering zone”, the outlet H_2 reached a steady state level, which was lower than the inlet H_2 . This is an evidence of reverse WGS reaction. At higher temperatures such as 600 °C (Fig. 5), the difference between inlet and outlet H_2 fraction was even larger, providing evidence of reverse WGS reaction. This means, during the rich operation, the concentration of H_2 was governed by the reverse WGS reaction. This observation indicates that OSC measurements are not recommended to be conducted based on H_2 consumption during rich period due to additional H_2 consumption by reverse WGS reaction. As a result, it is better to measure the OSC during lean period. In order to predict the H_2 concentration, a reversible WGS reaction was added in the OSC model. It was reported that WGS mechanism on $CeZrO_x$ supported PGM catalysts proceeds through a redox mechanism involving PGM and ceria and the reactions of Ce_2O_3 with H_2O and CO_2 (Eqs. (1) and (2)) are playing important roles in WGS and steam reforming of HCs [64,65]. Therefore, a global kinetic model for WGS reaction was proposed by lumping the active sites of ceria and PGM together. The rate expression of WGS reaction is given in Eq. (17), which was taken from [63]. The kinetic parameters are tabulated in Table 2. Fig. 6 shows the outlet H_2 fractions when H_2 reaches steady state during rich period at different temperatures. Predicted H_2 fractions as well as experimental data both showed that H_2 reached equilibrium. This observation further demonstrates the importance of reverse WGS reaction and it is necessary to include it in OSC modeling.

Interestingly, formation of H_2 was observed in Fig. 4 and Fig. 5 when the feeding gas was switched from rich to lean right after 60 s. Similar observation was reported by Moller et al. in a TWC [24]. The H_2 formation is a result of catalyst re-oxidation by H_2O as H_2O was presented in both rich and lean operations. In other words, the reduction of CeO_2 by H_2 or CO is reversible and needs to be taken into account in the model.

$$R_{wgs} = \frac{k_{wgs} c_{CO} c_{H_2O}}{(1 + K_{CO} c_{CO})(1 + K_{H_2} c_{H_2})} \left(1 - \frac{c_{H_2} c_{CO_2}}{c_{H_2O} c_{CO} K_{wgs,eq}} \right) \quad (17)$$

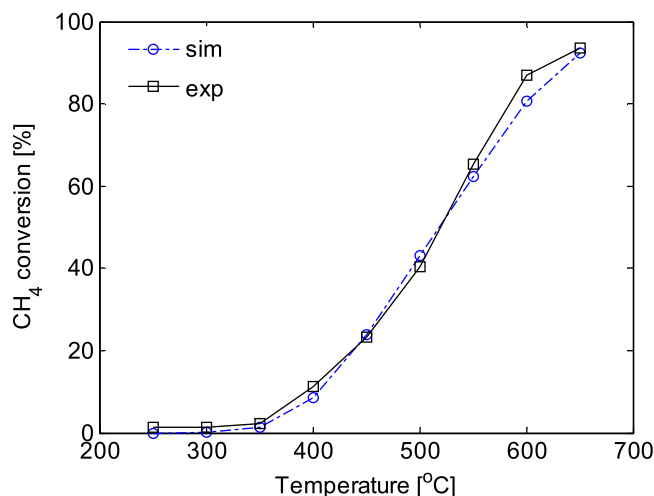


Fig. 10. CH_4 conversion during CH_4/O_2 pulsing experiments at different temperatures.

4.2. OSC with CO as a reductant

To investigate the effects of different reductants, OSC measurements were also taken by using CO as the reductant. Similar to the OSC measurements by using H_2 as a reductant, CO and O_2 were alternatively fed into the TWC catalyst. Fig. 7 shows the comparison of the oxygen fractions between the model and experiments conducted at 400 °C and the model successfully predicted the dynamic oxygen fraction at the catalyst outlet.

Similarly, in order to investigate the dynamic change of oxygen storage, cumulative oxygen storage calculated by is shown in Fig. 8. The cumulative OSC profiles showed two distinct regimes as expected, which were very similar to the case of H_2 . However, in the fast OSC storage regime, a temperature dependence was evidently observed. In the kinetic controlled regime, a higher catalyst temperature resulted in higher oxygen storage. Moreover, the oxygen storage on the surface ceria site was far from saturation at 250 °C, since the amount of OSC at 250 °C was much lower than the OSC at 400 °C in the fast O_2 uptake regime. The increase of OSC on the surface site at higher temperature is due to oxygen lattice diffusion from sub-surface site. This temperature dependence of OSC was modeled through thermodynamic equilibrium between Ce_2O_3 and CeO_2 on the sub-surface ceria site during CeO_2 reduction under rich conditions.

4.3. OSC with CH_4 as a reductant

H_2 and CO are the most active reducing agents for OSC depletion. However, there is a significant amount of CH_4 in the natural gas engine exhaust, which cannot be neglected. In order to investigate the reducibility of OSC with respect to CH_4 . In the next experiment CH_4 was used as the reductant during lean/rich cycling.

When the temperature was below 350 °C, there was small amount of oxygen storage that was close to zero. This indicates that CH_4 was not active in reacting with CeO_2 below 350 °C, which is quite different from H_2 and CO. Since there was no CeO_2 reduction by CH_4 below 350 °C, no OSC could be measured during lean period. Fig. 9 shows the cumulative oxygen storage at 350 °C, 400 °C, 450 °C and 500 °C. As temperature increased to 400 °C, CH_4 started to light off due to steam reforming reaction. CH_4 was converted to H_2 and CO, which are active reductants to reduce CeO_2 during the rich period as above-mentioned, resulting in measurable OSC during lean period. Fig. 10 shows the CH_4 conversion due to steam reforming reaction at different temperatures. CH_4 steam reforming

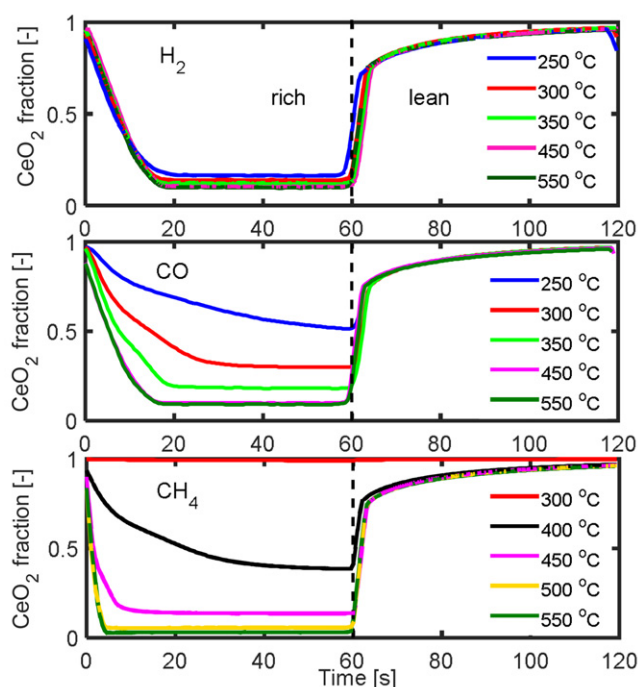


Fig. 11. Simulated fraction of CeO_2 using H_2 , CO and CH_4 as reductants at different temperatures.

reaction is therefore necessary to be incorporated in the OSC model for natural gas engines. The rate expression of CH_4 steam reforming is shown in Eq. (18) and the kinetic parameters are summarized in Table 2.

$$R_{\text{sr}} = k_{\text{wgs}} c_{\text{CH}_4} \left(1 - \frac{c_{\text{CO}} c_{\text{H}_2}^3}{c_{\text{CH}_4} c_{\text{H}_2\text{O}} K_{\text{sr,eq}}} \right) \quad (18)$$

Also, the correlation between the amount of OSC and CH_4 conversion is interesting. From Fig. 9, the OSC significantly increases from 400 °C to 450 °C but increase much less from 450 °C to 500 °C, while the increase of CH_4 conversion is similar over the temperature window of 400 °C–500 °C. This indicates that CH_4 conversion is not directly correlated to the amount of OSC. In other words, the amount of OSC is not a limiting factor for CH_4 reforming. This can be further supported by the fact that OSC becomes flat above 500 °C (in Fig. 12), while CH_4 conversion increases from 40% at 500 °C to 90% at 650 °C.

4.4. Temperature dependence

It is widely reported that OSC is strongly dependent on temperature [4,7]. Unlike ammonia storage on zeolite materials, in which the storage capacity decreases with temperature [34,66], the OSC increases with temperatures. The migration of oxygen lattice or vacancy between surface precious metal and ceria and sub-surface ceria is an activated process [4,7]. As temperature increases, the rate of oxygen lattice diffusion increases. Moreover, reduction of ceria is an equilibrium phenomena [24], which indicates that the degree of reduction of ceria is controlled by temperature. As a result, the OSC increases with temperature at the beginning. As temperature further increases, the OSC may stay flat or decrease depending on the thermodynamic properties of ceria. The temperature dependence on the OSC in the model is accounted by the degree of CeO_2 reduction. The overall coverage of CeO_2 (surface CeO_2 and sub-surface CeO_2) at different temperatures from simulations are given in Fig. 11. During CeO_2 reduction with the presence of H_2 , CO or CH_4 , a higher degree of CeO_2 reduction was reached as tempera-

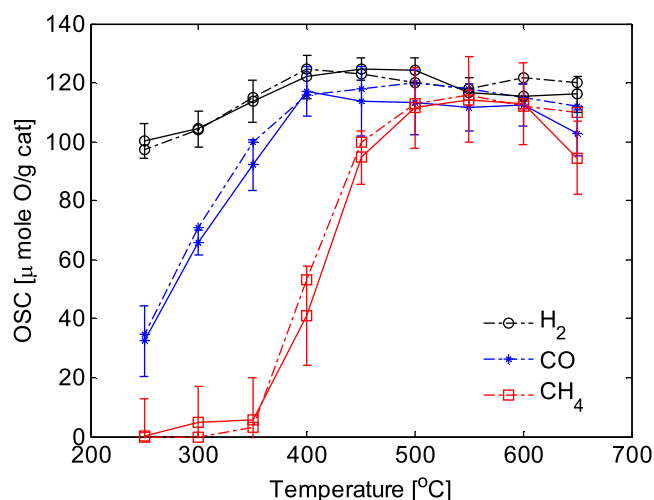


Fig. 12. Amount of dynamic oxygen storages (integrated over 20s during lean period) using H_2 , CO and CH_4 as reductants as a function of temperature (dash line: model; solid line: experiments with uncertainties).

ture increases. However, the coverage of CeO_2 does not go to zero even at 650 °C as CeO_2 was not fully reduced to Ce_2O_3 with the presence of H_2O . In the oxygen storage period, the coverages of CeO_2 are very similar at different temperatures. This is the result of a constant temperature independent diffusion coefficient used in the model, which is consistent with the cumulative OSC curves in Fig. 3, Fig. 8 and Fig. 9. In Fig. 11, the same CeO_2 fraction indicates that a similar state of ceria during oxygen storage rather than the same amount of OSC. The amount of OSC is actually determined by the difference in the CeO_2 fraction between the start of lean period and the end of lean period. In other words, reduction of ceria during rich is the limiting step for the amount of OSC.

The temperature effects on dynamic OSC were analyzed for different reductants. The cumulative OSC with a duration of 20 s in the lean period were chosen to represent the dynamic OSC for comparison. The reasons that we selected 20 s are listed below: 1) 20 s is far beyond the lean period of dithering or fuel-cut events during realistic engine operations; 2) at around 20 s, more than 90% of the total OSC measured in the experiments were reached.

$$\text{OSC}_{20\text{s}} = \frac{SV}{m_{\text{cat}}} \int_{t=60\text{s}}^{t=80\text{s}} 2 (c_{\text{O}_2,\text{in}} - c_{\text{O}_2,\text{out}}) \frac{PV_{\text{cat}}}{RT} dt \quad (19)$$

As shown in Fig. 12, there was slight temperature dependence of oxygen storage by using H_2 as the reductant. On the other hand, the amount of OSC by using CO and CH_4 as reductants showed stronger temperature dependence, especially below 400 °C. It is worthwhile to notice that, in the case of CO and CH_4 , H_2 is expected to be formed through WGS reaction or steam reforming and subsequently reduce OSC. Generally, H_2 is the most active reducing species due to the highest measured OSC at 250 °C compared to that of CO and CH_4 . The reducibility of reductants on OSC decreases in the order of $\text{H}_2 > \text{CO} > \text{CH}_4$. However, the amount of OSC reached at the very similar level when temperature was higher than 400 °C. WGS and steam reforming reactions are quite active at temperatures above 400 °C, the generated active species like H_2 and CO actually narrows down the difference in OSC by using different reductants. Also, it should be noticed that the shape of the curves in Fig. 12 will not change with a longer integration period for OSC calculation in Eq. (19). However, the absolute value of OSC will increase slightly if a longer integration duration was used.

5. Conclusions

A dual-site OSC model was developed to predict the dynamic oxygen storage on a TWC catalyst. Two oxygen storage sites (surface ceria and sub-surface ceria) were found to be necessary to model the two distinct regimes of the oxygen storage process. A shrinking core diffusion approach was applied on the sub-surface site to model the slow oxygen storage and depletion. Thermodynamically consistent kinetics were obtained through calibration from experimental OSC measurements. From both experiments and modeling, WGS reaction and steam reforming reaction were found to play significant roles in determining the amount of OSC and therefore were incorporated in the OSC model. The amount of OSC with different types of reductant was compared. OSC measured with H_2 showed a slight temperature dependence, followed by CO and CH_4 . The reducibility of reductants on OSC decreased in the order of $H_2 > CO > CH_4$ at the temperature from 250 °C to 450 °C. However, similar amount of OSC was observed at temperature above 450 °C regardless of the types of reductant. With the dual-site OSC model, the instantaneous oxygen concentration as well as the dynamic oxygen storage could be correctly predicted. Moreover, this OSC model can be incorporated into a full TWC model to predict the dynamic performance of TWCs.

Appendix A. Derivation of reaction rate expression of oxygen storage on sub-surface ceria

The schematic of the representative “shrinking core” of ceria is shown in Fig. A.1. This shrinking core diffusion model is used to describe oxygen lattice diffusion from the surface ceria to the sub-surface ceria.

The diffusion rate of oxygen from surface to the sub-surface can be described by:

$$R_{diff} = D (4\pi r^2) \Omega_2 \frac{dc_{O_2}}{dr} \quad (A.1)$$

The surface reaction rate of oxygen storage on the sub-surface is calculated by:

$$R_{react} = k \cdot \Omega_2 \cdot c_{O_2,rs} (1 - \theta_2) \cdot A_s \quad (A.2)$$

At the interface between surface CeO_2 and subsurface Ce_2O_3 , the diffusion rate is equal to reaction rate:

$$\frac{4\pi D}{l_f} \Omega_2 (c_{O_2,rt} - c_{O_2,rs}) \cdot r_t \cdot r_s = k \cdot \Omega_2 \cdot c_{O_2,rs} (1 - \theta_2) * 4\pi r_s^2 \quad (A.3)$$

The oxygen concentration at the interface of surface CeO_2 and sub-surface Ce_2O_3 is calculated as:

$$c_{O_2,rs} = \frac{c_{O_2,rt}}{1 + k \frac{d_p}{D} \frac{r_s}{r_t}} \quad (A.4)$$

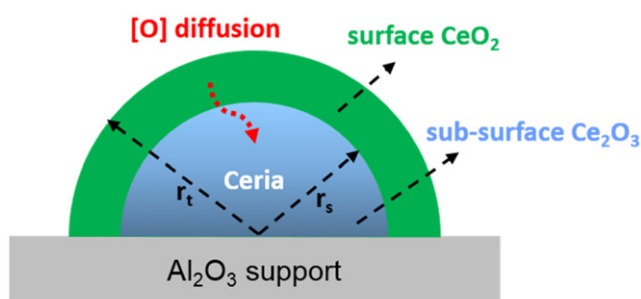


Fig. A.1. Schematic of shrinking core diffusion model.

Therefore, the rate expression for oxygen storage on the sub-surface site can be derived by substituting Eq. (A.4) into Eq. (A.2):

$$R_{O_2,sub} = k_{eff} c_{O_2} \Omega_2 (1 - \theta_2) \quad (A.5)$$

with an effective rate constant

$$k_{eff} = \frac{k}{1 + k \left[1 - (1 - \theta_2)^{1/3} \right] l_f} \quad (A.6)$$

where l_f is the thickness of the ceria surface and is calculated based on the relationship $l_f = r_t - r_s = r_t \left[1 - (1 - \theta_2)^{1/3} \right]$ and $\frac{r_s}{r_t} = (1 - \theta_2)^{1/3}$.

References

- [1] H.M. Cho, B.-Q. He, Energy Convers. Manag. 48 (2007) 608–618.
- [2] H.S. Gandhi, G.W. Graham, R.W. McCabe, J. Catal. 216 (2003) 433–442.
- [3] J. Gong, C. Rutland, SAE Tech. Pap. (2013), <http://dx.doi.org/10.4271/2013-01-1311>, 2013-01-1311.
- [4] A. Trovarelli, Catal. Rev. 38 (1996) 439–520.
- [5] R. Di Monte, J. Kašpar, Catal. Today 100 (2005) 27–35.
- [6] E. Aneggi, M. Boaro, C. De Leitenburg, G. Dolcetti, A. Trovarelli, J. Alloys Compd. 408–412 (2006) 1096–1102.
- [7] H.C. Yao, Y.F.Y. Yao, J. Catal. 86 (1984) 254–265.
- [8] M. Boaro, F. Giordano, S. Recchia, V. Dal, M. Giona, A. Trovarelli, Appl. Catal. B Environ. 52 (2004) 225–237.
- [9] N. Kamiuchi, M. Haneda, M. Ozawa, Catal. Today 201 (2013) 79–84.
- [10] N. Kamiuchi, M. Haneda, M. Ozawa, Catal. Today 232 (2014) 179–184.
- [11] P. Fornasiero, J. Kaspar, M. Graziani, J. Catal. 167 (1997) 576–580.
- [12] M. Daturi, E. Finocchio, C. Binet, J.C. Lavalley, F. Fally, V. Perrichon, J. Phys. Chem. B 103 (1999) 4884–4891.
- [13] J. Kaspar, P. Fornasiero, M. Graziani, Catal. Today 50 (1999) 285–298.
- [14] P. Fornasiero, R. Di Monte, R. Ranga, J. Kaspar, S. Meriani, A. Trovarelli, M. Graziani, J. Catal. 151 (1995) 168–177.
- [15] C. Li, K. Domen, K. Maruya, T. Onishi, J. Am. Chem. Soc. 111 (1989) 7683–7687.
- [16] C. Brinkmeier, G. Eigenberger, S. Buchner, A. Donnerstag, SAE Tech. Pap. (2003), <http://dx.doi.org/10.4271/2003-01-1001>, 2003-01-1001.
- [17] P. Kumar, I. Makki, J. Kerns, K. Grigoriadis, M. Franchek, V. Balakotaiah, Chem. Eng. Sci. 73 (2012) 373–387.
- [18] G.C. Koltsakis, P. a. Konstantinidis, A.M. Stamatelos, Appl. Catal. B Environ. 12 (1997) 161–191.
- [19] D. Tsinoglou, G. Koltsakis, J.P. Jones, Ind. Eng. Chem. Res. 41 (2002) 1152–1165.
- [20] D. Tsinoglou, G. Koltsakis, Chem. Eng. Sci. 58 (2003) 179–192.
- [21] G.N. Pontikakis, G.S. Konstantas, A.M. Stamatelos, J. Eng. Gas Turbines Power 126 (2004) 906–923.
- [22] J. Gong, C. Rutland, SAE Tech. Pap. (2013), <http://dx.doi.org/10.4271/2013-01-1572>, 2013-01-1572.
- [23] R. Holder, M. Bollig, D.R. Anderson, J.K. Hochmuth, Chem. Eng. Sci. 61 (2006) 8010–8027.
- [24] R. Möller, M. Votsmeier, C. Onder, L. Guzzella, J. Gieshoff, Appl. Catal. B Environ. 91 (2009) 30–38.
- [25] D. Chatterjee, O. Deutschmann, J. Warnatz, Faraday Discuss. 119 (2001) 371–384.
- [26] S.B. Kang, S.J. Han, I.-S. Nam, B.K. Cho, C.H. Kim, S.H. Oh, Chem. Eng. J. 241 (2014) 273–287.
- [27] H.J. Kwon, J. Hyun Baik, Y. Tak Kwon, I.-S. Nam, S.H. Oh, Chem. Eng. Sci. 62 (2007) 5042–5047.
- [28] L.S. Mukadi, R.E. Hayes, Comput. Chem. Eng. 26 (2002) 439–455.
- [29] P. Koci, M. Kubicek, M. Marek, Catal. Today 98 (2004) 345–355.
- [30] P. Koci, M. Kubicek, M. Marek, Ind. Eng. Chem. Res. 43 (2004) 4503–4510.
- [31] A. Yezerets, N.W. Currier, D.H. Kim, H. a. Eadler, W.S. Epling, C.H.F. Peden, Appl. Catal. B Environ. 61 (2005) 120–129.
- [32] J. Li, N. Currier, A. Yezerets, H.Y. Chen, H.S. Hess, SAE Tech. Pap. (2009), <http://dx.doi.org/10.4271/2009-01-0275>, 2009-01-0275.
- [33] S.Y. Park, K. Narayanaswamy, S.J. Schmiege, C.J. Rutland, Ind. Eng. Chem. Res. 51 (2012) 15582–15592.
- [34] J. Gong, K. Narayanaswamy, C.J. Rutland, Ind. Eng. Chem. Res. 55 (2016) 5874–5884.
- [35] H. Santos, M. Costa, Chem. Eng. J. 148 (2009) 173–183.
- [36] S.Y. Joshi, M.P. Harold, V. Balakotaiah, Chem. Eng. Sci. 65 (2010) 1729.
- [37] S. Bedrane, C. Descorme, D. Duprez, Catal. Today 73 (2002) 233–238.
- [38] M. Boaro, M. Vicario, C.D. Leitenburg, G. Dolcetti, A. Trovarelli, Catal. Today 77 (2003) 407–417.
- [39] C. Padeste, N.W. Cant, D.L. Trimm, Catal. Lett. 18 (1993) 305–316.
- [40] F. Sadi, D. Duprez, F. Gerard, A. Miloudi, J. Catal. 213 (2003) 226–234.
- [41] S. Abanades, A. Legal, A. Cordier, G. Peraudeau, G. Flamant, A. Julbe, J. Mater. Sci. 45 (2010) 4163–4173.
- [42] K. Otsuka, M. Hatano, A. Morikawa, J. Catal. 79 (1983) 493–496.
- [43] S. Sharma, S. Hilaire, J.M. Vohs, R.J. Gorte, H.-W. Jen, J. Catal. 190 (2000) 199–204.

- [44] J.E. Miller, M.D. Allendorf, R.B. Diver, L.R. Evans, N.P. Siegel, J.N. Stuecker, J. Mater. Sci. 43 (2008) 4714–4728.
- [45] S. Abanades, A. Legal, A. Cordier, G. Peraudeau, G. Flamant, A. Julbe, J. Mater. Sci. 45 (2010) 4163–4173.
- [46] S. Abanades, G. Flamant, Sol. Energy 80 (2006) 1611–1623.
- [47] S.M. Schimming, G.S. Foo, O.D. LaMont, A.K. Rogers, M.M. Yung, A.D. D'Amico, C. Sievers, J. Catal. 329 (2015) 335–347.
- [48] M. Zhao, M. Shen, J. Wang, J. Catal. 248 (2007) 258–267.
- [49] J.S. Hepburn, E. Thanasiu, D.A. Dobson, W.L. Watkins, SAE Tech. Pap. 962051 (1996), <http://dx.doi.org/10.4271/962051>.
- [50] L. Olsson, R.J. Blint, E. Fridell, Global kinetic model for lean NO_x traps, Ind. Eng. Chem. Res. 44 (2005) 3021–3032.
- [51] G. Colon, F. Valdivieso, M. Pijolat, R.T. Baker, J.J. Calvino, S. Bernal, Catal. Today 50 (1999) 271–284.
- [52] A. Holmgren, D. Duprez, B. Andersson, J. Catal. 182 (1999) 441–448.
- [53] A.B. Mhadeshwar, H. Wang, D.G. Vlachos, Phys. Chem. B 107 (2003) 12721–12733.
- [54] C. Karakaya, R. Otterstatter, L. Maier, O. Deutschmann, Appl. Catal. A: Gen. 470 (2014) 31–44.
- [55] J. Libuda, I. Meusel, J. Hoffmann, J. Hartmann, L. Piccolo, C.R. Henry, H.J. Freund, J. Chem. Phys. 114 (2001) 4669–4684.
- [56] C.E. Hori, H. Permana, K.Y.S. Ng, A. Brenner, K. More, K.M. Rahmoeller, D. Belton, Appl. Catal. B Environ. 16 (1998) 105–117.
- [57] B.C.H. Steele, J.M. Floyd, Proc. Br. Ceram. Trans. 72 (1971) 55–75.
- [58] A. Galdikas, C. Descorme, D. Duprez, F. Dong, H. Shinjoh, Top. Catal. 30/31 (2004) 405–409.
- [59] G. Zhou, P.R. Shah, T. Kim, P. Fornasiero, R.J. Gorte, Catal. Today 123 (2007) 86–93.
- [60] G. Zhou, P.R. Shah, T. Montini, P. Fornasiero, R.J. Gorte, Surf. Sci. 601 (2007) 2512–2519.
- [61] S. Huang, L. Li, J. Vleugels, P. Wang, O. Van Der Biest, J. Eur. Ceram. Soc. 23 (2003) 99–106.
- [62] D.D. Wagman, W.H. Evans, V.B. Parker, R.H. Schumm, I. Halow, Natl. Stand. Ref. Data Syst. (1982).
- [63] S. Hilaire, X. Wang, T. Luo, R.J. Gorte, J. Wagner, Appl. Catal. A Gen. 215 (2001) 271–278.
- [64] R.J. Gorte, S. Zhao, Catal. Today 104 (2005) 18–24.
- [65] J. Sun, J. Desjardins, J. Buglass, K. Liu, Int. J. Hydrogen Energy 30 (2005) 1259–1264.
- [66] K. Kamasamudram, N.W. Currier, X. Chen, A. Yezerets, Catal. Today 151 (2010) 212–222.